Major mouse placental compartments revealed by diffusion-weighted MRI, contrast-enhanced MRI, and fluorescence imaging

Eddy Solomon[a,1], Reut Avni[b,1], Ron Hadas[b], Tal Raz[b,c], Joel Richard Garbow[d], Peter Bendel[e], Lucio Frydman[a,2], and Michal Neeman[b,2]

Departments of [a]Chemical Physics, [b]Biological Regulation, and [e]Chemical Research Support, Weizmann Institute of Science, Rehovot, 76100 Israel; [c]Koret School of Veterinary Medicine, The Hebrew University of Jerusalem, Rehovot, 76100 Israel; and [d]Biomedical Magnetic Resonance Laboratory, Mallinckrodt Institute of Radiology, Washington University, St. Louis, MO 63110

Edited by R. Michael Roberts, University of Missouri, Columbia, MO, and approved June 4, 2014 (received for review January 27, 2014)

Mammalian models, and mouse studies in particular, play a central role in our understanding of placental development. Magnetic resonance imaging (MRI) could be a valuable tool to further these studies, providing both structural and functional information. As fluid dynamics throughout the placenta are driven by a variety of flow and diffusion processes, diffusion-weighted MRI could enhance our understanding of the exchange properties of maternal and fetal blood pools—and thereby of placental function. These studies, however, have so far been hindered by the small sizes, the unavoidable motions, and the challenging air/water/fat heterogeneities, associated with mouse placental environments. The present study demonstrates that emerging methods based on the spatiotemporal encoding (SPEN) of the MRI information can robustly overcome these obstacles. Using SPEN MRI in combination with albumin-based contrast agents, we analyzed the diffusion behavior of developing placentas in a cohort of mice. These studies successfully discriminated the maternal from the fetal blood flows; the two orders of magnitude differences measured in these fluids' apparent diffusion coefficients suggest a nearly free diffusion behavior for the former and a strong flow-based component for the latter. An intermediate behavior was observed by these methods for a third compartment that, based on maternal albumin endocytosis, was associated with trophoblastic cells in the interphase labyrinth. Structural features associated with these dynamic measurements were consistent with independent intravital and ex vivo fluorescence microscopy studies and are discussed within the context of the anatomy of developing mouse placentas.

robust diffusion MRI | high-field placental MRI | placental ADC maps | multimodal imaging

The placenta is an essential, versatile organ, providing life support for the developing fetus. The placenta's wide range of physiological functions include imposing an immunological barrier between the fetus and the mother; mediating the transfer of respiratory gases, water, ions, and nutrients; and producing and secreting an array of hormones, cytokines, and signaling molecules (1, 2). Mice are often used for studying these complex systems and serve as developmental and functional models to understand human pregnancy, as both species have a hemochorial placenta exhibiting similar transport mechanisms (3, 4). The mature placenta in mice is established by embryonic day (E) 10.5 and, like most primates' placentas, it is composed of three main layers: a maternal layer involving the decidua and the maternal vasculature, a layer of trophoblast cells, and a labyrinth facilitating exchanges between the maternal and fetal circulations (Fig. 1) (3, 5). Blood arriving from the maternal spiral arteries converges via straight canals into the placenta and from that point diverges into pools in the intervillous spaces within the labyrinth; those are interdispersed among fetal vessels, thus ensuring an efficient exchange between the two blood systems. Maternal blood vessels in the labyrinth are lined by layers of trophoblast cells that play a variety of important roles in exchanges of nutrients, gases, and waste; in the segregation of hormones; and in placental anchoring (3, 6–8). Fetal blood flows through an endothelial-cell–lined vascular bed with a tree-like hierarchy of vessel sizes, the smallest of which are micrometer sized (Fig. 1*A*) (3). It follows from this description that complex flow dynamics control the movement and transfer of fluids and nutrients within and between the different placental compartments; some of these are driven by microcirculation and others by active transport or passive diffusion (Fig. 1*B*).

Consequently, further understanding of placental functions and dysfunctions clearly requires measuring dynamic aspects of placental blood volume and blood flow, as well as their relation to features of the maternal–placental–fetal structures. Ex vivo analyses of histological sections are limited in this regard, because although capable of providing detailed structural information, they are compromised by the lack of functional dynamic information. Hence noninvasive in vivo imaging modalities in general—and imaging of placental mouse structures in particular—are essential for obtaining this kind of information and for understanding their connection to healthy and diseased fetal developments. Because of its noninvasive and potentially high-resolution nature, magnetic resonance

Significance

Fluid motion measurements can provide valuable insight regarding the structure and function of developing placentas. This study presents to our knowledge the first MRI characterization of multicompartmental diffusion and incoherent flow in pregnant mice at different gestation stages, made possible by methods herein introduced for the single-scan acquisition of diffusion-encoded images in the challenging environment associated with in vivo embryonic studies. These methods were combined with a customized contrast agent to reveal a freely diffusive maternal blood pool, a strongly perfused fetal blood flow, and an intermediate behavior for the trophoblastic labyrinth cell layer. Structural features associated with these dynamics were corroborated with ex vivo fluorescence microscopy and are discussed within the context of the anatomical structure of developing mouse placentas.

Author contributions: E.S., R.A., L.F., and M.N. designed research; E.S. and R.A. performed research; E.S., R.A., R.H., T.R., J.R.G., and P.B. contributed new reagents/analytic tools; E.S., R.A., L.F., and M.N. analyzed data; and E.S., R.A., L.F., and M.N. wrote the paper.

The authors declare no conflict of interest.

This article is a PNAS Direct Submission.

Freely available online through the PNAS open access option.

[1] E.S. and R.A. contributed equally to this work.

[2] To whom correspondence may be addressed. E-mail: lucio.frydman@weizmann.ac.il or michal.neeman@weizmann.ac.il.

This article contains supporting information online at www.pnas.org/lookup/suppl/doi:10.1073/pnas.1401695111/-/DCSupplemental.

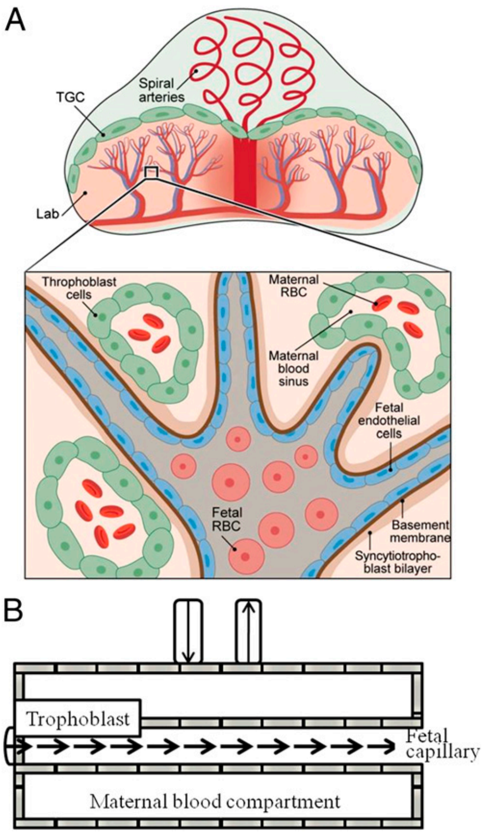

Fig. 1. Schematic diagrams summarizing (*A*) the structure and main components of a mouse placenta and (*B*) the movement of fluids in each of these main compartments as visualized by diffusion MRI. Inset in *A* details the fetal–maternal–trophoblastic interactions in the labyrinth (Lab) area: Fetal cells are surrounded by endothelial cells and membranes; fetal capillaries are surrounded by maternal blood sinuses, which conduct red blood cells (RBC) and are lined by trophoblast cells. Fluid exchanges between the fetal capillaries and the maternal blood pools are mediated by the trophoblasts, including the trophoblast giant cells (TGC).

imaging (MRI) could play a unique role in these characterizations of placental structures and their dynamics. Considering the small sizes of the cells and blood vessels involved in mouse placentas, ranging from 15 μm to 300 μm (3), it is beyond the realm of standard MRI methods to directly distinguish and resolve different compartments within an image. Still, MRI can offer a unique window for understanding tissue function and morphology at the microscopic level if used for measuring molecular diffusion and blood microcirculation—for instance, by relying on diffusion-weighted (DW) pulsed-field gradient methods (9–12). DW MRI is a sensitive approach to map the incoherent motions of water molecules and thus provide insight into tissue microstructures at the micrometer level (13, 14) based on measurements of so-called apparent diffusion coefficients (ADCs). ADC values reflect various types of movements beyond free water diffusivity, including blood microcapillary flow, morphological restrictions acting on the molecular diffusion, and perfusion effects. This endows DW MRI with the ability to monitor changes in fluid mobility under different physiological conditions, a feature that has been applied to assess human placental structures in normal and in high-risk pregnancies (15, 16). Particularly promising in this regard are intravoxel incoherent motions methods, which attempt to distinguish between diffusion and perfusion of fluids (17, 18). These methodologies have been previously applied to assess placentas in normal and pathological conditions, both in human and in rat models (19–22).

Retrieving reliable diffusion measurements by MRI requires overcoming potential artifacts from fetal and maternal motions. Therefore, diffusion analyses are based on "ultrafast" methods such as spin-echo echo-planar imaging (SE-EPI) (15, 20–22), capable of delivering the 2D imaging information being sought in a single shot. EPI's capabilities, however, are limited when applied to imaging internal organs, subject to unavoidable motions and sizable magnetic field distortions (23–26). Placental DW imaging, particularly at the high magnetic fields required to analyze mouse-sized structures, further exacerbates these in vivo imaging challenges: Single-shot measurements then need to confront the tissue heterogeneities that characterize mouse internal organs in general and fat-rich abdominal regions in particular, as well as the continuous fetal motion and the constant cardiac and breathing motions of the anesthetized dam. These challenges have hitherto prevented the characterization of diffusion and perfusion properties in mouse placentas. On the other hand, it has been recently shown that emerging single-shot MRI methods based on spatiotemporal encoding (SPEN) principles can cope with the spatial, chemical, and field heterogeneities that normally challenge EPI (27, 28). In addition, SPEN allows one to acquire reliable ADC maps (29), making it a particularly attractive tool for exploring diffusion-weighted MRI studies in challenging systems such as mouse placentas. The aim of this study was to exploit diffusion-encoded SPEN (dSPEN) acquisition strategies, to uncover structural and dynamic aspects of in vivo placentas during various gestation periods in pregnant mice. These studies were carried out in the presence and absence of a high-molecular-weight contrast agent, biotin-bovine serum albumin–gadolinium diethylene triamine pentacetate (b-BSA-GdDTPA), which allowed us to fractionate the diffusion behavior for different placental vasculatures. The versatility of these in vivo MRI analyses was further complemented with histological and microscopic fluorescence identifications, leading to insights regarding in vivo supra- and subvoxel morphologies, diffusion, and perfusion in placentas.

Results

Imaging Mouse Placentas by SPEN and SE-EPI MRI. To evaluate the diffusion information that can be obtained from placental structures in mice, the imaging performances of single-shot SE-EPI and SPEN were first compared. MRI images were acquired on pregnant mice at gestation days E14.5 ($n = 2$ mice; five placentas) and E18.5 ($n = 3$ mice; seven placentas), using 2D fast spin echo as an anatomical reference (Fig. 2*A*), single-shot 2D SPEN (Fig. 2*B*), and 2D SE-EPI (Fig. 2*C*). Both SE-EPI and SPEN uncover several fetuses, although the latter does so with higher sensitivity (Fig. 2 *D* and *E*). Placental anatomic features are much less preserved in the SE-EPI images collected for the remaining pregnant mice, whereas their SPEN counterparts provided better agreement with the multiscan results (more examples in Fig. S1). Signal-to-noise ratios (SNRs) calculated

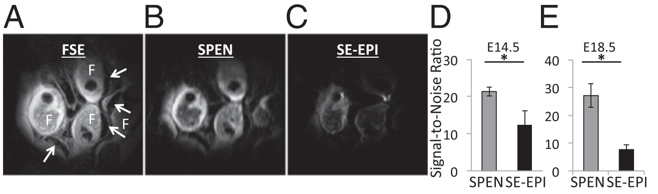

Fig. 2. Anatomical images of a pregnant mouse showing multiple feto-placental units. F marks the fetuses and the white arrows their placentas. (*A*) A 2D fast spin-echo (FSE) image. (*B*) A 2D SPEN image. (*C*) A 2D SE-EPI image. (*D* and *E*) Signal-to-noise ratio of SPEN and SE-EPI images on embryonic days 14.5 (*D*) and 18.5 (*E*) (mean ± SEM; $^{*}P < 0.05$). Scanning parameters: 1 mm slice thickness, field of view (FOV) = 40×40 mm^2, and in-plane resolution = 0.1563 mm (*A*) and 0.4 mm (*B* and *C*). Both 2D SPEN and SE-EPI data were collected with one segment and reconstructed with no zero filling. Only 50% of the EPI images succeeded in supplying usable data (additional SPEN and SE-EPI MRI data can be found in Fig. S1).

for each placenta and averaged over the total number of placentas for each gestation day were also significantly higher in SPEN MRI over SE-EPI experiments; for E18.5, SPEN = 27 ± 4, SE-EPI = 7.6 ± 1.7, $P < 0.05$; and for E14.5, SPEN = 21.3 ± 1.2, SE-EPI = 12.3 ± 3.7, $P < 0.05$.

When seeking to target a small organ such as a mouse placenta, it is valuable to choose a restricted region of interest (ROI) within the sensitive volume of the surface coil—without having to reposition the mouse or the coil. Given SPEN's non-Fourier nature, this can be executed along this technique's low-bandwidth direction simply by restricting its frequency-swept range. These "zooming" abilities of SPEN—normally absent in SE-EPI and FSE acquisitions—are illustrated in Fig. 3; these enabled us to focus on smaller fields of view and generate ADC maps with improved intraplacental resolution.

Placental ADCs: Overall Features and Gestation Dependence. With these anatomical imaging tools as a starting point, placental ADC values were measured along three orthogonal directions (readout, phase-encode/SPEN, and slice selection). In those cases where SE-EPI provided reasonable images, no statistically significant differences were found between the mean ADCs afforded by this method and those by the diffusion-encoding SPEN techniques ($P = 0.45$). The latter, more robust dSPEN experiments were thus used to explore basic features about placental ADCs. The mean ADC for an ROI including the entire placenta at E18.5 ($n = 10$ mice; 39 placentas) was found to be $2.9 \pm 0.6 \times 10^{-3}$ mm^2/s, derived using a monoexponential fitting of the data. The experimental data (Fig. 4) revealed a nonlinearity in the logarithmic signal decay plots, suggesting fast- and slow-decaying compartmental fractions consistent with a biexponential attenuation $\mathrm{SI}/\mathrm{SI}(0) = F_{\mathrm{fast}} e^{-b\mathrm{ADC}_{\mathrm{fast}}} + F_{\mathrm{slow}} e^{-b\mathrm{ADC}_{\mathrm{slow}}} + c$. Similar results have also been reported in the literature for rat and human placentas (19–22). Biexponential fits of data acquired with a finer increment in the b values were carried out on a subset of $n = 5$ mice, 19 placentas; these suggested the presence of two fractions with populations $F_{\mathrm{fast}} = 37 \pm 13\%$ and $F_{\mathrm{slow}} = 63 \pm 16\%$ and ADCs of $250 \pm 100 \times 10^{-3}$ mm^2/s and $2.2 \pm 0.6 \times 10^{-3}$ mm^2/s, respectively. When applying these biexponential fits, however, the overall R^2 values improved by less than 3% over their monoexponential counterparts. This highlights the challenges of these simple fitting procedures for resolving the multiple compartments that are present in the placenta's complex structure.

In following up with another aspect examined in human placentas (16), dSPEN was also used to explore for potential correlations between ADC values and mouse placental aging. Two gestation days, 3 d after placental formation (E14.5, $n = 6$ mice; 19 placentas) and toward the end of pregnancy (E18.5, $n = 10$ mice; 39 placentas), were evaluated. We found no statistical difference between the placental ADC values for the two gestation ages (mean ADC for the E14.5 mice = $2.4 \pm 0.9 \times 10^{-3}$ mm^2/s; $P = 0.065$).

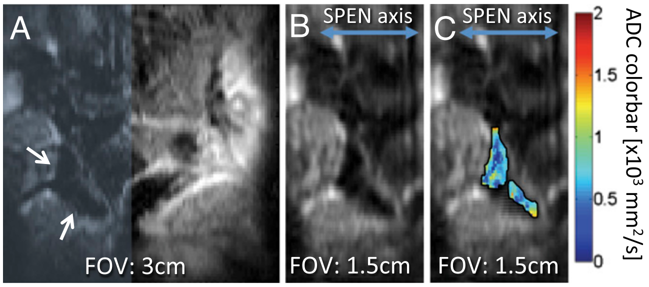

Fig. 3. Representative example of SPEN's zooming abilities, illustrated on a 2-mm slice containing mouse placentas on E18.5. (*A*) SPEN magnitude image on the full (30 × 30 mm^2) FOV. (*B*) Restricted FOV (15 × 30 mm^2, resolution = 0.15 × 0.3 mm^2), corresponding to the shaded area in *A*. (*C*) ADC maps of two placentas indicated by the arrows in *A*, overlaid on top of the zoomed SPEN image.

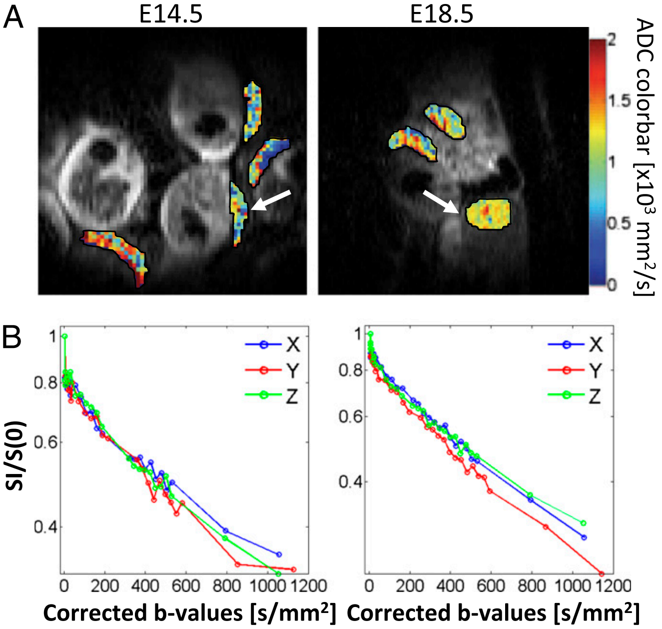

Fig. 4. Changes in placental ADC during pregnancy. (*A*) Comparison of ADC maps measured on a mouse at gestation ages E14.5, ~3 d after the placental formation, and at E18.5, toward the end of pregnancy. (*B*) Corresponding diffusion semilog plots measured at the two ages for the placentas indicated by the arrows in *A*. Measurements were repeated for a large array of *b* values (shown here corrected due to potential self- and cross-terms between the diffusion and the imaging gradients) in the search for biexponentiality; data are shown as repeated for gradients applied along the *x*, *y*, and *z* axes, corresponding to the readout, SPEN, and slice-selection directions, respectively. Measurements carried out for $n = 10$ dams and 39 placentas, revealed only a marginal change in the ADC between the two gestation dates.

Resolving Subvoxel Placental Structures Using a Multicomponent Fitting. As mentioned, placental circulation can be roughly described as composed of a maternal vascular system lined with trophoblast cells and a fetal system involving small blood capillaries. MRI in general, and dSPEN measurements in particular, do not have the ability to spatially resolve these major morphological subdivisions within the mouse placentas, due to the small sizes of the cells and blood vessels they involve. Biexponential fits of the DW MRI data (Fig. 4*B*) also lack the ability to discern these structures with confidence—despite the fact that all major placental circulation systems are expected to possess different diffusion and perfusion properties. These structures, however, could become distinguishable by executing suitable ADC measurements before and after administration of b-BSA-GdDTPA. As reported, this high-molecular-weight relaxation agent administered i.v. to the dam will enter the maternal circulation but cannot penetrate into the fetal circulation (30). Hence, after b-BSA-GdDTPA administration, the ADCs in maternal and fetal compartments could be differentiated by repeating the dSPEN measurements at long and short repetition times (TRs): At long TRs both compartments would be observed, whereas at short TRs only the rapidly relaxing maternal system would be detected. Moreover, following its administration, b-BSA-GdDTPA is actively internalized into the trophoblast's layer (Fig. S2) where it creates a T_2*-shortening effect (30). Therefore, following the administration of this contrast agent, the signals arising from this compartment should disappear completely. In view of these considerations, we hypothesize that the placental signal attenuation observed when diffusion is measured at long TR and before the administration of the contrast agent can be described as the sum of three contributing components,

$$\frac{\mathrm{SI}_1}{\mathrm{SI}_1(0)} = \left(F_{\mathrm{mat}} e^{-b\mathrm{ADC}_{\mathrm{mat}}} + F_{\mathrm{fet}} e^{-b\mathrm{ADC}_{\mathrm{fet}}} + F_{\mathrm{Tro}} e^{-b\mathrm{ADC}_{\mathrm{Tro}}}\right) + c, \qquad [1]$$

where $\mathrm{ADC}_{\mathrm{mat}}$, $\mathrm{ADC}_{\mathrm{fet}}$, and $\mathrm{ADC}_{\mathrm{Tro}}$ are the ADCs in the maternal vasculature, the fetal vasculature, and trophoblasts, respectively, and F_{mat}, F_{fet}, and F_{Tro} represent the different compartmental fractions. By contrast, the same experiment repeated for long TR but after administration of b-BSA-GdDTPA will, due to the T_2* darkening effect acting on the trophoblasts, be given by

$$\frac{\mathrm{SI}_2}{\mathrm{SI}_2(0)} = \left(F_{\mathrm{mat}} e^{-b\mathrm{ADC}_{\mathrm{mat}}} + F_{\mathrm{fet}} e^{-b\mathrm{ADC}_{\mathrm{fet}}}\right) + c. \qquad [2]$$

Finally, if the same contrast-enhanced experiment is repeated with short TR, the dominant compartment contributing to the placental signal intensity will be the maternal vasculature, weighted by a postagent longitudinal relaxation rate R_1:

$$\frac{\mathrm{SI}_3}{\mathrm{SI}_3(0)} = \left[F_{\mathrm{mat}} e^{-b\mathrm{ADC}_{\mathrm{mat}}} \left(1 - e^{-\mathrm{TR}\cdot R_1}\right)\right] + c. \qquad [3]$$

Maternal R_1 values can be determined separately from ancillary contrast-enhanced MRI experiments (2.5 s^{-1} on average) and hence their weighting factor is known, as is the fixed volume fraction $F_{\mathrm{mat}} + F_{\mathrm{fet}} + F_{\mathrm{Tro}} = 1$ condition. It follows from these relations that the relative fractions of all three intravoxel placental components can be distinguished by using such a contrast-aided DW approach.

With this model as background, changes in the placental signal intensity before and after administration of b-BSA-GdDTPA were analyzed for short (250 ms) and long (5,000 ms) TR acquisitions. The former measurements lead, after their fitting to Eq. **3**, to F_{mat} and $\mathrm{ADC}_{\mathrm{mat}}$ estimates. This $\mathrm{ADC}_{\mathrm{mat}}$ served as an initial value for the fitting of the long-TR contrast-enhanced diffusion data: Biexponential fitting of Eq. **2** thus allowed us to extract the $\mathrm{ADC}_{\mathrm{fet}}$, F_{mat} and F_{fet} values. In a last step, both $\mathrm{ADC}_{\mathrm{mat}}$ and $\mathrm{ADC}_{\mathrm{fet}}$ as well as the $F_{\mathrm{mat}}/F_{\mathrm{fet}}$ ratio were used to fit long-TR data collected in the absence of the contrast agent; Eq. **1** thus allowed us to derive $\mathrm{ADC}_{\mathrm{Tro}}$ and all of the relative fractions. An example of this multiple-relaxation curve analysis is presented in Fig. 5*A*. This analysis revealed that maternal blood constitutes 66 ± 8%, fetal blood is 24 ± 6%, and the trophoblasts are 10 ± 6% of the overall placental volume (Fig. 5*B*). ADCs were found to be 3.1 ± 0.4, 240 ± 30, and $19 \pm 7 \times 10^{-3}$ mm^2/s for maternal, fetal, and trophoblastic compartments, respectively (Fig. 5*C*). Note that the first two among these populations are reminiscent of the ratios obtained from the biexponential fits. Placental fraction maps were calculated on a pixel-by-pixel basis, providing a clear spatial distribution between the different compartments (Fig. 5 *D*–*F*).

Optical Imaging of Mouse Placentas. To validate these in vivo dSPEN-based compartmental characterizations, fetal and maternal placental blood vessels were also differentiated using optical ex vivo imaging. This method used two different fluorescent dyes: BSA-ROX and fluorescein (Fig. 6). BSA labeled with 6-carboxy-X-rhodamine (BSA-ROX) is confined to the maternal vasculature (30), whereas fluorescein, a small fluorescent agent, crosses the placental barrier and penetrates both the maternal and the fetal circulation within the placenta. This feature is exemplified in Fig. 6 *A*, *D*, and *E*, where ex vivo fluorescent optical analyses show the expected penetration of fluorescein into both fetal and maternal circulation, whereas BSA-ROX remains confined in the maternal circulation within the labyrinth. Maternal and fetal blood volumes derived on the basis of this discrimination proceeded as described in *SI Text* (Fig. S3), and led to 104 ± 6.3 µL and 46 ± 6.5 µL volumes, respectively. According to these estimates the maternal and fetal fractions are thus 69 ± 4% and 31 ± 4%, respectively, in good agreement with the DW MRI-derived data.

Discussion

Diffusion-Weighted Placental MRI: Methodological Considerations. Over the past years, the use of genetically modified mice having targeted defects in the placental structure and function has significantly enhanced our understanding of embryonic and placental development (5, 6). Many placental phenotypes have been related to vascular pathologies, including changes in blood volume and flow mechanisms; therefore, understanding the specific partition and hemodynamics of maternal and fetal blood volumes as well as the organization of the feeding maternal arteries is key to elucidating placental function. Although ex vivo analyses can provide detailed information into placental structures, their dynamic insight is limited, and in vivo methods are essential for such functional analyses. In vivo multiphoton microscopy, for instance, allows one to examine placental microcirculation; however, it requires surgical exposure of the placenta unit, thereby compromising its function, and requires euthanizing the mice at the end of each procedure, thereby preventing longitudinal examinations throughout the gestation (31, 32). Microultrasound also provides a valuable noninvasive tool to quantify placental growth and hemodynamics, yet suffers from spatial inaccuracies depending on a placenta's instantaneous orientation and cannot scan all feto-placental units simultaneously,

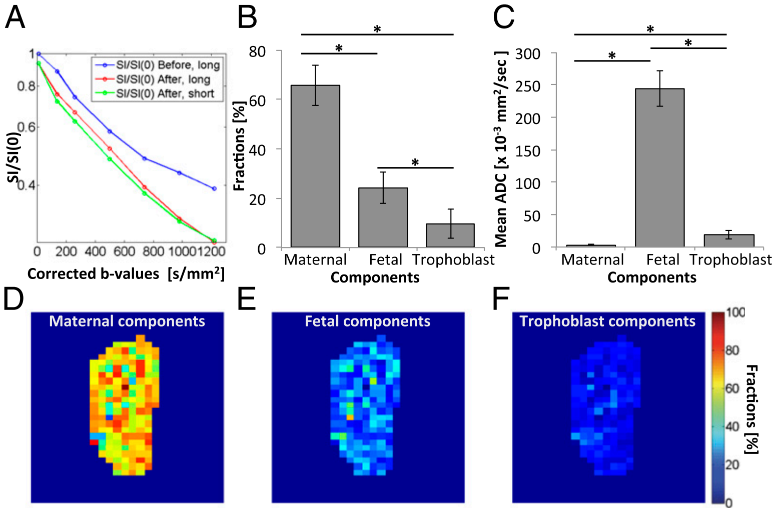

Fig. 5. Resolving placental structures using contrast-enhanced dSPEN MRI. (*A*) Representative multiexponential diffusion log plots obtained before and after the administration of b-BSA-GdDTPA, at short (250 ms) and long (5,000 ms) recycle times, TR. (*B* and *C*) Estimation of the different placental compartmental fractions (*B*) and of the corresponding ADC values (*C*) (mean ± SEM; **P* < 0.05), performed as described in the main text. (*D*–*F*) Example of placental fraction maps showing the relative maternal (*D*), fetal (*E*), and trophoblastic (*F*) contributions, discriminated on the basis of mean ADC fits implemented pixel-by-pixel. According to this analysis, maternal, fetal, and trophoblastic contributions constitute 64.4%, 23.7%, and 11.9% of overall placental volume, respectively, in agreement with bulk placental measurements based on Eqs. **1**–**3**.

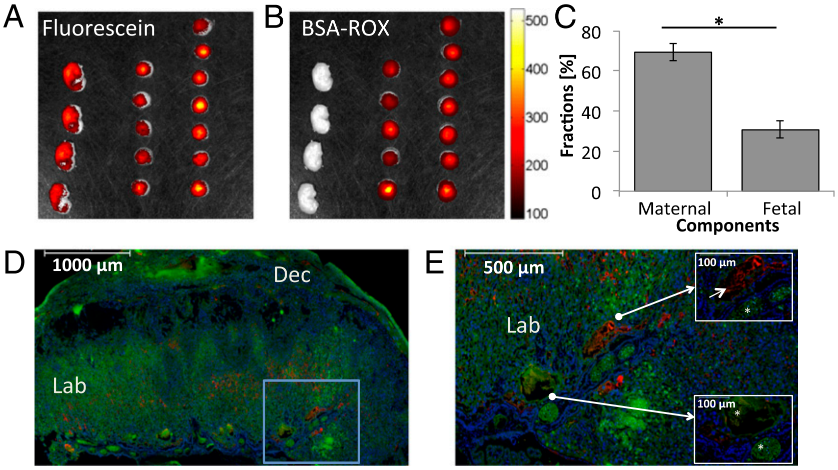

Fig. 6. Optical imaging of maternal and fetal blood fractions on ICR pregnant mice. (*A* and *B*) Fluorescence intensity analyzed using an IVIS imaging system following the injection of fluorescein (*A*) and BSA-ROX (*B*). These ex vivo analyses involved $n = 6$ dams and 27 placentas/fetuses. (*C*) Estimated maternal and fetal blood fractions derived for a cohort of placentas from this optical microscopy analysis (mean ± SEM; $P < 0.05$). (*D* and *E*) Representative fluorescence images of placental histology sections, showing the circulatory bed of the placental labyrinth. BSA-ROX (red) was confined to the maternal circulation within the labyrinth, whereas fluorescein (green) also penetrated the fetal circulation. Markers in *D* and *E* represent 1,000 μm and 500 μm, respectively. Blue frame in *D* is magnified in *E*, whereas *Insets* in *E* indicate the localization of a maternal blood pool (*Upper Right*; marker indicates 100 μm) as well as fetal blood spaces (*Lower Left*; asterisks in *Insets* mark the fetal blood spaces and marker indicates 100 μm). Blue: Hoechst-stained nuclei. Dec, decidua; Lab, labyrinth.

thereby facing serious limitations in the study of transgenic mouse models (33–36). By contrast, MRI is fully noninvasive and is especially well suited for analyzing pregnancy in large litter species such as mice, as the entire uterus can in principle be imaged in a single scan. Establishing diffusion-oriented MRI methods for these in vivo fetal examinations, however, is challenging due to the presence of motion artifacts, including periodic movements like maternal respiration—which could be compensated by synchronized "triggered" acquisitions—as well as nonperiodic movements including fetal translation and rotation, gastrointestinal contractions, and uterine contractions. These motions pose general problems in diffusion-based experiments, which are further confounded in the abdomen by the presence of heterogeneous tissue/air and fat/water interfaces. The magnetic susceptibility differences are further aggravated at the high magnetic fields that are needed to analyze placentas with sufficient sensitivity in small animals like mice. The data presented here demonstrate the capability of diffusion-encoded SPEN-based MRI methods, for successfully dealing with these major challenges.

With the aid of SPEN, ADC values could be measured for mouse placenta; these fell in the $\sim 2.9 \pm 0.9 \times 10^{-3}$ mm^2/s range, slightly higher but comparable in dispersion to the $0.5–2.5 \times 10^{-3}$ mm^2/s range that was previously reported for human placentas (16, 37) and larger than the average ADC = 0.9 ± 0.3 reported for rats (19). The first of these studies also revealed a decrease in placental ADCs from 2.2 to 0.7×10^{-3} mm^2/s in humans over the course of weeks 20–40 of gestation if a $b = 0$ value was included in the ADC measurement, but no statistically significant progression if $b \geq 50$ s/mm^2 was the initial point—presumably due to the filtering out of perfusion effects. The latter studies, by contrast, found no significant correlations between ADCs and human placental aging. Our measurements of mean placental ADCs at two gestation stages (E14.5 and E18.5) also lacked, within statistical variability, a definite trend in ADC with aging.

Previous studies on human placentas (20–22) indicated biexponentiality in the *b*-value plots, suggestive of a faster ADC contribution arising from capillary flow. In the present study, we observed a measure of biexponentiality, suggesting a larger slowly diffusing population, and a minority fraction with significantly higher mobility. Although the existence of these two populations could not be conclusively proved for the analyzed cohort, it is tempting to establish a parallel between the 70/30 population split extracted from these fits and the similar partition between maternal and fetal vasculature extracted by the more reliable contrast-enhanced measurements summarized in Fig. 5.

Placental DW MRI: Compartmentalization Insight. Placentas are heterogeneous organs containing two independent blood circulation systems, fetal and maternal, which are in close proximity in the labyrinth area. Both maternal and fetal blood circulation and diffusion are controlled by different mechanisms and presumably should contribute to discernable ADC values. As mentioned, however, even the availability of quality diffusion MRI data did not allow us to unambiguously distinguish between these ADC values, using multiexponential fits. This is not surprising given that the voxel volumes are relatively large, the distribution of velocities present within them is heterogeneous, and the vessels show a variety of intravoxel orientations. To extract the internal placental compartments and estimate their fraction sizes we therefore complemented dSPEN with a contrast-enhanced MRI approach, using the high-molecular-weight albumin-based contrast agent b-BSA-GdDTPA. Using this approach we were able to obtain structural and functional information beyond the pixel-size resolution. The changes in the placental signal intensity before and after administration of this contrast agent, repeated at short and long TRs, yielded a clear fractionation of the placenta into its major constituents. The maternal blood constitutes approximately two-thirds of the placental volume, the fetal volume was *ca.* one-quarter, and the various trophoblastic components completed the rest. These volumetric findings were supported and validated using ex vivo fluorescence imaging of i.v. administered fluorescent probes.

In vivo studies also revealed relatively large ADCs for the trophoblast cells and especially large values for the fetal vasculature, vis-à-vis the maternal diffusion rates. This reflects the different flow patterns that probably occur in these different blood spaces. Fluids from the maternal spiral arteries converge via straight canals to the intervillous spaces (3); according to our measured ADC values, this fluid's behavior resembles the one anticipated for freely diffusing water at 37 °C. This is to be expected given the nature of these villi. Fetal vessels, by contrast, are structured to bathe these structures with a rapid convection of fluids, to ensure adequate exchanges of nutrients. Judging from the fetal ADC values that we measured, exceeding the maternal counterparts by orders of magnitude, these movements are dominated by flow rather than by passive diffusion. Finally trophoblast cells, which experience a large degree of exchange of water molecules between the fetal and maternal systems, reflect an intermediate ADC value. The fact that these ADC values are still considerably higher than those expected for free diffusion suggests that it is not intracellular water but rather contributions of fluid being actively filtered across the fetal–maternal barrier. By imposing the derived ADC values for each compartment, maps of the apparent volume fraction distribution of each placental compartment could be calculated (Fig. 5). These quantitatively defined microcirculation and diffusion features are consistent with known descriptions of placental anatomy (Fig. 1). According to these, maternal blood enters the labyrinth via large arterial canals, relatively unobstructed vessels for which fluid motion thus appears dominated by free diffusion. By contrast, the flow inside the fetal capillaries is fast and consistent with the need to ensure proper nutrients transfer; the high ADC values reported in Fig. 5 reflect this perfusion-driven microcirculation. Finally, trophoblast cells line the lumen of maternal vessels and mediate fetal/maternal filtration of water, consistent with their intermediate ADC value.

Conclusions

Emerging MRI methods like SPEN provide a powerful imaging alternative for investigating anatomical and dynamic features even under the challenging conditions arising in in vivo MRI of mice at high magnetic fields. Equipped with this tool, diffusion-based studies capable of enhancing our understanding of placental structure and function become possible. As shown in this work, the combination of dSPEN and MRI using high-molecular-weight contrast agents succeeded in resolving multiple placental compartments and in characterizing them both in their fractions—which were validated by independent optical means—and in their apparent diffusion/flow characteristics. This kind of work opens valuable possibilities for phenotyping specific placental alterations, including longitudinal studies monitoring fluid exchanges in healthy and mutant mice throughout the gestation period. Such analyses, as well as extensions of SPEN studies to larger animals, to higher-resolution isotropic and anisotropic diffusion MRI measurements, and to other spectroscopy probes—both thermal and hyperpolarized—are in progress.

Materials and Methods

Animal Models. All experiments were approved by the Institutional Animal Care and Use Committee of the Weizmann Institute of Science. Female ICR mice were studied in these experiments. MRI scans involved a total of $n = 12$ dams and 52 placentas/fetuses; optical imaging studies were done on $n = 6$ dams and 27 placentas/fetuses. Animals were analyzed on E14.5 and E18.5 of the pregnancy. Timed mating was carried out by pairing strain-matched males and females overnight, with the following morning designated as E0.5 if a vaginal plug was detected as indication that mating had occurred.

MRI and Optical Imaging Protocols. MRI experiments were performed at 9.4 T on a 94/20 USR Biospec scanner (Bruker). Ex vivo optical imaging experiments were carried out on placentas after removing them from the animals; their fluorescent signals were analyzed using an IVIS 100 Imaging System (Xenogen). Full details on these MRI and optical imaging protocols are given in *SI Text* and Fig. S3.

ACKNOWLEDGMENTS. We thank Dr. Inbal Biton for discussions and assistance with these experiments. Financial support is from the Seventh Framework European Research Council Advanced Grant 246754-ULTRANMR, a Helen and Kimmel Award for Innovative Investigation, and the generosity of the Perlman Family Foundation (to L.F.); the Seventh Framework European Research Council Advanced Grant 232640-IMAGO (to M.N.); and Grant 2011405 from the US–Israel Binational Science Foundation (to M.N., J.R.G., and T.R.). M.N. is an incumbent of the Helen and Morris Mauerberger Chair in Biological Sciences.

1. Carter AM (2012) Placenta: Predicting future health. *Placenta* 33(Suppl):S1.
2. Desforges M, Sibley CP (2010) Placental nutrient supply and fetal growth. *Int J Dev Biol* 54(2–3):377–390.
3. Adamson SL, et al. (2002) Interactions between trophoblast cells and the maternal and fetal circulation in the mouse placenta. *Dev Biol* 250(2):358–373.
4. Rossant J, Cross JC (2001) Placental development: Lessons from mouse mutants. *Nat Rev Genet* 2(7):538–548.
5. Watson ED, Cross JC (2005) Development of structures and transport functions in the mouse placenta. *Physiology* 20:180–193.
6. Cross JC (2000) Genetic insights into trophoblast differentiation and placental morphogenesis. *Semin Cell Dev Biol* 11(2):105–113.
7. Hemberger M, Cross JC (2001) Genes governing placental development. *Trends Endocrinol Metab* 12(4):162–168.
8. Zybina EV, Zybina TG (1996) Polytene chromosomes in mammalian cells. *Int Rev Cytol* 165:53–119.
9. Beaulieu C (2002) The basis of anisotropic water diffusion in the nervous system - a technical review. *NMR Biomed* 15(7–8):435–455.
10. Callaghan PT (1993) *Principles of Nuclear Magnetic Resonance Microscopy* (Clarendon, Oxford).
11. Neeman M, Freyer JP, Sillerud LO (1990) Pulsed-gradient spin-echo diffusion studies in Nmr Imaging - effects of the imaging gradients on the determination of diffusion-coefficients. *J Magn Reson* 90(2):303–312.
12. Roberts TP, Schwartz ES (2007) Principles and implementation of diffusion-weighted and diffusion tensor imaging. *Pediatr Radiol* 37(8):739–748.
13. Le Bihan D (2003) Looking into the functional architecture of the brain with diffusion MRI. *Nat Rev Neurosci* 4(6):469–480.
14. Shemesh N, Ozarslan E, Basser PJ, Cohen Y (2010) Detecting diffusion-diffraction patterns in size distribution phantoms using double-pulsed field gradient NMR: Theory and experiments. *J Chem Phys* 132(3):034703.
15. Bonel HM, et al. (2010) Diffusion-weighted MR imaging of the placenta in fetuses with placental insufficiency. *Radiology* 257(3):810–819.
16. Manganaro L, et al. (2010) MRI and DWI: Feasibility of DWI and ADC maps in the evaluation of placental changes during gestation. *Prenat Diagn* 30(12–13):1178–1184.
17. Le Bihan D, et al. (1986) MR imaging of intravoxel incoherent motions: Application to diffusion and perfusion in neurologic disorders. *Radiology* 161(2):401–407.
18. Le Bihan D, Turner R (1992) The capillary network: A link between IVIM and classical perfusion. *Magn Reson Med* 27(1):171–178.
19. Alison M, et al. (2013) Use of intravoxel incoherent motion MR imaging to assess placental perfusion in a murine model of placental insufficiency. *Invest Radiol* 48(1): 17–23.
20. Moore RJ, et al. (2000) In vivo intravoxel incoherent motion measurements in the human placenta using echo-planar imaging at 0.5 T. *Magn Reson Med* 43(2):295–302.
21. Moore RJ, et al. (2008) Spiral artery blood volume in normal pregnancies and those compromised by pre-eclampsia. *NMR Biomed* 21(4):376–380.
22. Moore RJ, et al. (2000) In utero perfusing fraction maps in normal and growth restricted pregnancy measured using IVIM echo-planar MRI. *Placenta* 21(7):726–732.
23. Buonocore MH, Gao L (1997) Ghost artifact reduction for echo planar imaging using image phase correction. *Magn Reson Med* 38(1):89–100.
24. Stehling MK, Turner R, Mansfield P (1991) Echo-planar imaging: Magnetic resonance imaging in a fraction of a second. *Science* 254(5028):43–50.
25. Twieg DB (1983) The k-trajectory formulation of the NMR imaging process with applications in analysis and synthesis of imaging methods. *Med Phys* 10(5):610–621.
26. Yang QX, et al. (2004) Reduction of magnetic field inhomogeneity artifacts in echo planar imaging with SENSE and GESEPI at high field. *Magn Reson Med* 52(6): 1418–1423.
27. Ben-Eliezer N, Shrot Y, Frydman L (2010) High-definition, single-scan 2D MRI in inhomogeneous fields using spatial encoding methods. *Magn Reson Imaging* 28(1): 77–86.
28. Tal A, Frydman L (2006) Spatial encoding and the single-scan acquisition of high definition MR images in inhomogeneous fields. *J Magn Reson* 182(2):179–194.
29. Solomon E, Shemesh N, Frydman L (2013) Diffusion weighted MRI by spatiotemporal encoding: Analytical description and in vivo validations. *J Magn Reson* 232:76–86.
30. Plaks V, et al. (2011) Functional phenotyping of the maternal albumin turnover in the mouse placenta by dynamic contrast-enhanced MRI. *Mol Imaging Biol* 13(3):481–492.
31. de Moraes LV, Tadokoro CE, Gómez-Conde I, Olivieri DN, Penha-Gonçalves C (2013) Intravital placenta imaging reveals microcirculatory dynamics impact on sequestration and phagocytosis of Plasmodium-infected erythrocytes. *PLoS Pathog* 9(1): e1003154.
32. Zenclussen AC, Olivieri DN, Dustin ML, Tadokoro CE (2012) In vivo multiphoton microscopy technique to reveal the physiology of the mouse placenta. *Am J Reprod Immunol* 68(3):271–278.
33. Foster FS, et al. (2002) A new ultrasound instrument for in vivo microimaging of mice. *Ultrasound Med Biol* 28(9):1165–1172.
34. Mu J, Slevin JC, Qu D, McCormick S, Adamson SL (2008) In vivo quantification of embryonic and placental growth during gestation in mice using micro-ultrasound. *Reprod Biol Endocrinol* 6:34.
35. Mu J, Adamson SL (2006) Developmental changes in hemodynamics of uterine artery, utero- and umbilicoplacental, and vitelline circulations in mouse throughout gestation. *Am J Physiol Heart Circ Physiol* 291(3):H1421–H1428.
36. Zhang J, Croy BA (2009) Using ultrasonography to define fetal-maternal relationships: Moving from humans to mice. *Comp Med* 59(6):527–533.
37. Sivrioglu AK, et al. (2013) Evaluation of the placenta with relative apparent diffusion coefficient and T2 signal intensity analysis. *Diagn Interv Radiol* 19(6):495–500.